OPEN ACCESS
IOP Publishing | Songshan Lake Materials Laboratory
Letters
Materials Futures
Mater. Futures **1** (2022) 031001 (8pp)
https://doi.org/10.1088/2752-5724/ac8947

Letter

Low Na-β''-alumina electrolyte/cathode interfacial resistance enabled by a hydroborate electrolyte opening up new cell architecture designs for all-solid-state sodium batteries

Marie-Claude Bay*, **Rabeb Grissa**, **Konstantin V Egorov**, **Ryo Asakura** and **Corsin Battaglia***

Empa, Swiss Federal Laboratories for Materials Science and Technology, Überlandstrasse 129, 8600
Dübendorf, Switzerland

E-mail: marieclaude.bay@empa.ch and corsin.battaglia@empa.ch

Received 3 May 2022, revised 8 August 2022
Accepted for publication 11 August 2022
Published 26 August 2022

Abstract

Development of low-resistance electrode/electrolyte interfaces is key for enabling all-solid-state batteries with fast-charging capabilities. Low interfacial resistance and high current density were demonstrated for Na-β''-alumina/sodium metal interfaces, making Na-β''-alumina a promising solid electrolyte for high-energy all-solid-state batteries. However, integration of Na-β''-alumina with a high-energy sodium-ion intercalation cathode remains challenging. Here, we report a proof-of-concept study that targets the implementation of a Na-β''-alumina ceramic electrolyte with a slurry-casted porous $NaCrO_2$ cathode with infiltrated sodium hydroborates as secondary electrolyte. The hydroborate $Na_4(B_{12}H_{12})(B_{10}H_{10})$ possesses similar sodium-ion conductivity of 1 mS cm^{-1} at room temperature as Na-β''-alumina and can be fully densified by cold pressing. Using the $Na_4(B_{12}H_{12})(B_{10}H_{10})$ secondary electrolyte as interlayer between Na-β''-alumina and $NaCrO_2$, we obtain a cathode-electrolyte interfacial resistance of only 25 Ω cm^2 after cold pressing at 70 MPa. Proof-of-concept cells with a sodium metal anode and a $NaCrO_2$ cathode feature an initial discharge capacity of 103 mAh g^{-1} at C/10 and 42 mAh g^{-1} at 1 C with an excellent capacity retention of 88% after 100 cycles at 1 C at room temperature. Ion-milled cross-sections of the cathode/electrolyte interface demonstrate that intimate contact is maintained during cycling, proving that the use of hydroborates as secondary electrolyte and as an interlayer is a promising approach for the development of all-solid-state batteries with ceramic electrolytes.

---

* Authors to whom any correspondence should be addressed.

2752-5724/22/031001+8$33.00

Supplementary material for this article is available online

Keywords: interface, all-solid-state battery, sodium metal anode, hydroborate electrolyte, Na-β''-alumina electrolyte

1. Introduction

All-solid-state batteries with a lithium or sodium metal anode are considered as next-generation batteries as they promise high energy density as well as enhanced operation safety by replacing the flammable liquid electrolyte used in lithium-ion batteries with an ideally non-flammable solid electrolyte [1–3]. While solid electrolytes with lithium- and sodium-ion conductivity comparable to liquid electrolytes have been developed, their integration into all-solid-state cells with stable interfaces enabling long-term cycling and high current densities remains challenging [4–6].

During the past decade, a major research focus has been on achieving stable solid electrolyte/alkali metal anode interfaces [7–11]. High interfacial resistance at the solid electrolyte/alkali metal anode interface leads to the formation and propagation of alkali metal dendrites upon battery charging, limiting the operation current density [12–15]. Some of us demonstrated low interfacial resistance <10 Ω cm^2 at the interface between a Na-β''-alumina ceramic electrolyte and a sodium metal anode, enabling current densities of 12 mA cm^{-2} at room temperature [16]. This achievement was possible by applying a high-temperature heat treatment of the Na-β''-alumina electrolyte in inert atmosphere to remove surface contamination responsible for the high interfacial resistance and for dendrites formation. Such high current densities meet fast-charging requirement [17], making Na-β''-alumina a promising candidate for all-solid-state batteries. In addition to demonstrated fast-charging capabilities, Na-β''-alumina ceramics exhibit a sodium-ion conductivity competitive with typical liquid electrolytes (1.2 mS cm^{-1} at room temperature), a wide electrochemical stability window (>3 V), and proven chemical stability against sodium metal [18–21].

However, the integration of ceramic electrolytes with high-energy intercalation cathodes remains challenging. Poor contact at the solid-solid interface results in large interfacial resistance and unsatisfactory electrochemical performance [22]. Sintering of ceramic composites including the electrolyte and the cathode active material may represent an option for zero-strain cathodes, which may avoid fracturing of the ceramic composite during electrochemical dis-/charge cycling. However, obtaining stable interfaces with low interfacial resistance by sintering remains challenging due to the elevated temperatures required to generate intimate contact between the electrolyte and cathode [23, 24]. Alternatively, cathode materials were integrated with ceramic electrolytes by employing liquid [25], gel [26, 27], or soft polymer [28–30] secondary electrolytes, which guarantee sufficient mechanical contact and low interfacial resistance.

In this study, we propose a novel strategy to contact a cathode to a rigid Na-β''-alumina ceramic electrolyte. Our approach employs a soft, non-flammable secondary solid electrolyte from the hydroborate class of materials to establish mechanical and ionic contact between the Na-β''-alumina primary electrolyte and a NaCrO$_2$ cathode. Hydroborates remain a relatively underexplored class of solid electrolytes with lithium- and sodium-ion conductivities on the order of 1 mS cm^{-1} at room temperature comparable to Na-β''-alumina, a wide electrochemical stability window of >3 V, and the unique property to fully densify by cold pressing [31–34]. However, hydroborate electrolyte-based all-solid-state batteries with sodium metal anodes are subject to sodium metal dendrites propagation unless high pressure is applied, limiting their operation to low current densities [34]. Some of us previously reported the infiltration and crystallization of hydroborate electrolytes in slurry-casted porous cathodes, enabling their application in all-solid-state batteries with negligible interfacial resistances [35, 36]. Our method is demonstrated in a proof-of-concept all-solid-state sodium metal cell using Na-β''-alumina as primary electrolyte, the hydroborate Na$_4$(B$_{12}$H$_{12}$)(B$_{10}$H$_{10}$) as secondary electrolyte and interlayer material, and NaCrO$_2$ as cathode material, resulting in a cathode-electrolyte interfacial resistance of only 25 Ω cm^2.

2. Methods

2.1. Na-β′′-alumina ceramic electrolyte preparation

Spray-dried lithium-stabilized Na-β''-alumina powders were synthesized from boehmite (AlO(OH)), lithium hydroxide (LiOH), and sodium carbonate (Na$_2$CO$_3$) by a solid-state route [37]. Green bodies in the form of 15.5 mm diameter discs were uniaxially pressed. Sintering was performed in static air in a high-temperature laboratory furnace (Carbolite Gero HTF 1700) for 5 min at 1600 °C applying a heating and cooling rate of 3 °C min^{-1}. To facilitate shrinkage and to avoid excessive sodium (and lithium) loss, samples were placed on a buffer green disc of the same Na-β''-alumina powder. Samples and buffer discs were encapsulated within a dense magnesium-spinel dome and a corresponding magnesium-spinel support disc [37]. A ratio of Na-β''-alumina mass (samples plus buffer disc) to encapsulated volume of 0.14 g cm^{-3} was kept constant [38]. The obtained pellets have a density of 97.6% ± 0.1% compared to the crystallographic density. The pellets were then ground plan-parallel and polished with increasingly finer sandpapers up to a final polish using a 1200 P sandpaper, which corresponds to a sand particle size of 15 μm. The polished pellets had a final thickness of 1.4 ± 0.3 mm. Microstructural analysis by scanning electron microscopy (SEM) (see figure S1) revealed a grain size in the μm range and a bimodal pore size distribution with coarse pores in 10 s of μm diameter and small pores in <1 μm

Future perspectives

Growing global battery demand has triggered research into post lithium-ion batteries such as all-solid-state lithium and sodium batteries, which promise higher energy density and increased operation safety. Oxide-based electrolytes have attracted growing attention due to high ionic conductivities comparable to liquid electrolytes and wide electrochemical stability windows. However, oxide-based electrolytes are hard and brittle ceramics, making them difficult to integrate into all-solid-state batteries with low interfacial resistances. The cathode-ceramic electrolyte interface is particularly challenging due to the solid-solid contact. Research work should focus not only on improving the physical contact but also address the chemical reactions at the newly formed interface during cycling. In addition, a better understanding of the electrochemical kinetics at the solid-solid interface is required to guide the design of all-solid-state batteries. Finally, lab-scale cells often use thick ceramic electrolytes with thicknesses in the millimeter range. Towards commercialization of high-energy all-solid-state batteries, focus should lay on decreasing the electrolyte size to a thickness of about 50 μm while maintaining mechanical integrity.

diamater. A detailed study of the microstructure was previously published by some of us [37]. Polished samples were heat treated in argon atmosphere for 3 h at 900 °C applying a heating rate of 4.2 °C min^{-1} to remove surface contamination in the form of carbon and hydroxyl groups, as described in [16].

2.2. Cathode preparation

$NaCrO_2$ was synthesized according to [38]. Cr_2O_3 (Sigma-Aldrich) and Na_2CO_3 (Sigma-Aldrich) were mixed for 15 min in a mortar. The powder mixture was pressed into a pellet and heat treated in argon atmosphere for 5 h at 900 °C. X-ray analysis as well as scanning electron micrographs of the as-synthesized $NaCrO_2$ powder are shown in figure S2. After passive cool down in argon, the resulting powder was ground in a mortar. The slurry for the cathode preparation consisted in the as-synthesized $NaCrO_2$ active material powder, polyvinylidene difluoride (PVDF) binder (KF1100, Kureha), and conductive carbon additives (Super C65, Imerys) in a 95:2:3 weight ratio using N-methyl-2-pyrrolidone as solvent. The slurry was tape-casted on an aluminum current collector with a mass loading between 3.1 and 6.5 mg cm^{-2} (see table S7). Discs of 12 mm diameter were punched out from the obtained cathode sheet, followed by drying under vacuum for 12 h at 120 °C.

2.3. Application of hydroborate interlayer and cell assembly

Hydroborate electrolyte precursors $Na_2B_{12}H_{12}$ and $Na_2B_{10}H_{10}$ were purchased from Katchem and prepared according to [34]. An equimolar ratio of the hydroborate precursors $Na_2B_{12}H_{12}$ and $Na_2B_{10}H_{10}$ were dissolved in anhydrous ethanol (>99.5% purity, Sigma-Aldrich) with a concentration of 100 mg ml^{-1}. An amount of 30 μl of this solution was drop casted on a porous $NaCrO_2$ cathode disc and on a Na-β''-alumina pellet. Both parts were left for about 10 min to allow infiltration of the hydroborate solution into the pores of the $NaCrO_2$ cathode and impregnation into the Na-β''-alumina electrolyte. The infiltrated $NaCrO_2$ cathode was then placed onto the impregnated Na-β''-alumina electrolyte, and the stack was left to dry overnight in protected atmosphere, followed by a heat treatment under vacuum at 180 °C to crystalize the highly ion-conducting phase of $Na_4(B_{12}H_{12})(B_{10}H_{10})$. A pressure of 70 MPa was finally applied on the stack to densify the crystallized hydroborate interlayer. For the sodium metal anode, a 10 mm disc was punched out of a ∼200 μm thick sodium metal foil. The sodium disc was mechanically scratched to remove the oxide layer before attachment onto the Na-β''-alumina electrolyte/$NaCrO_2$ cathode stack. Cells were cycled under an initial stack pressure of 3.4 MPa. At this pressure, the sodium metal anode spreads to a diameter of ∼12 mm covering the whole area of a Na-β''-alumina pellet on one side.

2.4. Materials characterization

Cross sections were prepared using a broad-beam argon-ion miller (Hitachi IM4000 Plus). For the Na-β''-alumina/cathode interface, the cut is performed using a stationary ion beam, where the sample swings around the center of alignment with an amplitude of 15° and a speed of 60 rpm. However, the cross section of the Na-β''-alumina/sodium interface was ion milled using softer conditions (amplitude of 30° and speed of 30 rpm) in order to preserve the sodium metal and prevent any possible melting. SEM was used to image the Na-β''-alumina/cathode interface (Hitachi S4800) and the Na-β''-alumina/Na metal interface (FEI Nova NanoSEM 230).

2.5. Electrochemical characterization

Electrochemical characterization was performed by a multichannel galvanostat/potentiostat (Biologic VSP) in home-built electrochemical cells allowing the application of pressure to the cell stack under argon atmosphere in a glovebox (MBraun). Electrochemical impedance spectroscopy (EIS) was conducted at frequencies between 0.1 Hz and 1 MHz with a 20 mV sinusoidal amplitude. Galvanostatic charge/discharge measurements were performed at increasing C-rates ranging from C/10 to 1 C (1 C = 120 mA g^{-1}) between 2 V and 3.6 V vs. Na^+/Na. Long-term cycling measurements were performed at a rate of 1 C between 2 V and 3.3 V vs. Na^+/Na to minimize hydroborate oxidation [33, 39]. Both experiments were conducted after a 12 h rest at room temperature (25 °C–30 °C) and EIS data were recorded after the end of discharge.

3. Results

Figure 1(a) illustrates and summarizes the cell assembly protocol described in detail in the previous section and figure 1(b) shows a sketch of the completed cell architecture. The full cell consists of a sodium metal anode, a Na-β''-alumina ceramic primary electrolyte serving as separator, a $Na_4(B_{12}H_{12})(B_{10}H_{10})$ interlayer acting also as secondary electrolyte that is infiltrated into the slurry-casted porous $NaCrO_2$ cathode. In this study, we choose $NaCrO_2$ as cathode active material for its proven fast-charging capabilities in liquid

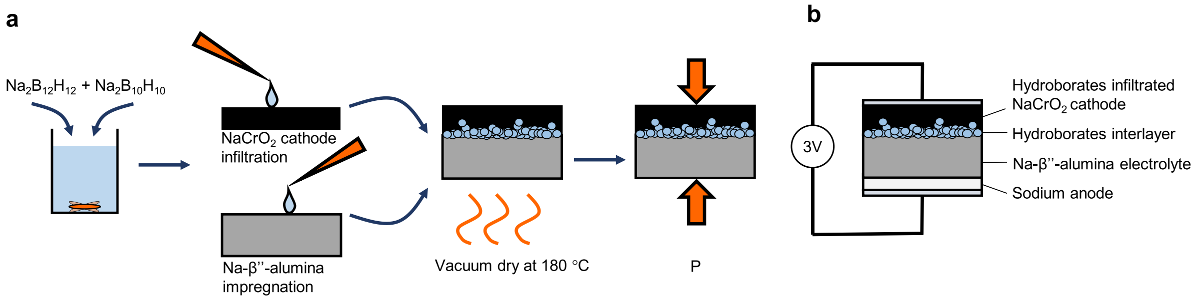

Figure 1. (a) Cell assembly protocol consisting of hydroborate electrolyte precursors salt dissolution into ethanol, $NaCrO_2$ cathode infiltration and Na-β''-alumina impregnation by drop casting, hydroborate electrolyte crystallization during vacuum drying, and interlayer densification by applying an external pressure. (b) Sketch of full cell architecture.

electrolytes [40], small volume expansion [41], and for its dis-/charge voltage profile that matches the electrochemical stability window of $Na_4(B_{12}H_{12})(B_{10}H_{10})$ (stable up to 3.25 V followed by slow, but not dramatic oxidation up to 3.6 V) and of Na-β''-alumina (stable up to about 3.6 V) [18, 39, 42, 43]. The theoretical capacity of $NaCrO_2$ is 120 mAh g^{-1} but reported practical reversible capacity reaches 110 mAh g^{-1} when cycled between 2 V and 3.6 V with a voltage plateau at around 3 V.

The densification step of the hydroborate interlayer is critical to obtain a low resistance at the Na-β''-alumina electrolyte-cathode interface. To study the impact of the densification pressure on the cell impedance, EIS was conducted on cells assembled with increasing densification pressures from 3 MPa to 87 MPa after releasing the pressure. Figure 2(a) shows representative Nyquist plots for the varying densification pressures and the corresponding equivalent circuits used to fit the data. Fitting results are summarized in tables S1–S4. For the cell assembled at the lowest pressure of 3 MPa, the corresponding Nyquist plot reveals the presence of three contributions that can be fitted using three RC elements in series. Based on the corresponding capacitance of 10^{-10} F, we ascribe the first semi-circle at an apex frequency of 1 MHz to Na-β''-alumina grain boundaries. Note that the Na-β''-alumina bulk contribution can be observed only at higher frequencies and lower temperatures [44, 45]. The $Na_4(B_{12}H_{12})(B_{10}H_{10})$ bulk contribution to the resistance is expected to be relatively small compared to the contribution of the Na-β''-alumina grain boundaries, due to the much lower thickness, and was not taken into consideration in the fit. With capacitances of 10^{-8} F and 10^{-7} F, we ascribe the second and third semicircles at apex frequencies of 30 kHz ($R = 192\ \Omega\ cm^2$) and 1 kHz ($R = 713\ \Omega\ cm^2$) to interfacial resistances. Because of the demonstrated negligible interfacial resistance $<8\ \Omega\ cm^2$ at the Na-β''-alumina/Na metal interface obtained using the heat treatment developed in [16], we ascribe the interfacial resistances to hydroborate/Na-β''-alumina and hydroborate/$NaCrO_2$ cathode interfaces. As the porous slurry-casted $NaCrO_2$ cathode provides a larger surface area than the dense Na-β''-alumina, which reduces the apparent interfacial resistance, we attribute the smaller semicircle at 30 kHz to the hydroborate/$NaCrO_2$ cathode interface and the larger semicircle at 1 kHz to the hydroborate/Na-β''-alumina interface. At an increased densification pressure of 43 MPa, the hydroborate/cathode contribution becomes negligible and only two contributions are observed including the Na-β''-alumina grain boundary contribution at 1 MHz and the hydroborate/Na-β''-alumina contribution at 1 kHz ($R = 251\ \Omega\ cm^2$). The interfacial resistance further decreases as the densification pressure increases and saturates at a minimum value of 25 $\Omega\ cm^2$ for an applied pressure $\geqslant$70 MPa. In fact, increasing the pressure to 90 MPa resulted in a similar value, as shown in figure S3. The decrease in interfacial resistance both at the hydroborate/Na-β''-alumina and hydroborate/$NaCrO_2$ cathode interfaces with increasing pressure can thus be directly explained by the densification of the hydroborate layer and the consequently improved ionic contact. The hydroborate interlayer acts thus as an ion-conductive contacting medium between the Na-β''-alumina ceramic electrolyte and the cathode which requires sufficiently high density to minimize interfacial resistances.

The saturation of the interfacial resistance at 25 $\Omega\ cm^2$ at pressure $\geqslant$70 MPa indicates that full compaction and good mechanical and ionic contact are obtained above this threshold pressure. The remaining interfacial resistance of 25 $\Omega\ cm^2$ may originate from pressure-independent contributions.

In figure 2(b), we investigate the impact of the processing solvent on the surface properties of Na-β''-alumina by EIS. We compare Nyquist plots of a Na-β''-alumina ceramic in contact with sodium metal electrodes after Na-β''-alumina heat treatment (figure 2(b) top) and after heat treatment followed by an extended exposure to the processing solvent anhydrous ethanol (figure 2(b) bottom). In both cases, the Na-β''-alumina was heat treated in order to reproduce the experimental conditions during cell assembly. The Nyquist plot obtained for the Na-β''-alumina ceramic after heat treatment reveals two contributions, which we ascribe to Na-β''-alumina grain boundaries at apex frequency of 1 MHz and to Na-β''-alumina/Na metal interface at apex frequency of 1 kHz ($R = 4\ \Omega\ cm^2$). Fitted parameters are summarized in tables S5 and S6. The low frequency tail <0.5 Hz, usually ascribed to an electrochemical reaction [46] e.g. from sodium stripping and plating, was excluded from the fit. After ethanol exposure, the Na-β''-alumina grain boundary contribution remains identical, while the interfacial contribution increases from 4 $\Omega\ cm^2$ to 50 $\Omega\ cm^2$. X-ray diffraction analysis conducted on heat-treated Na-β''-alumina

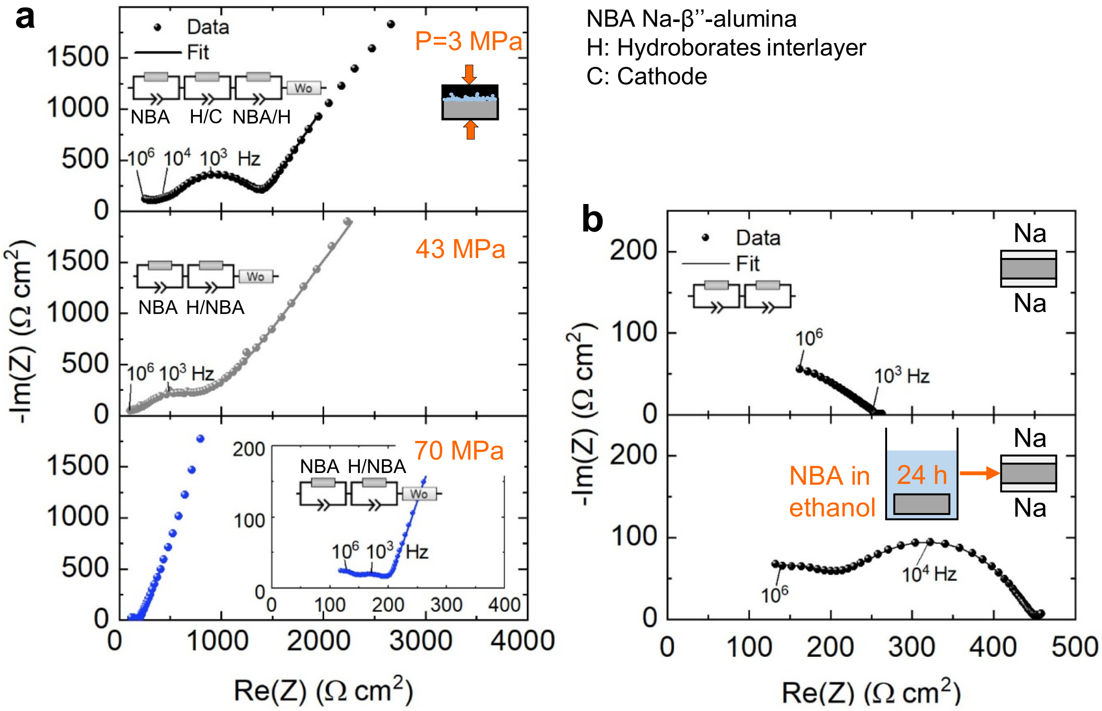

Figure 2. Impact of densification pressure on Na-β''-alumina/cathode interfacial resistance at room temperature. (a) Representative Nyquist plots for full cells assembled with different densification pressures. (b) Nyquist plots of symmetrical Na metal/Na-β''-alumina/Na metal cells assembled after Na-β''-alumina heat treatment (top) and after heat treatment followed by 24 h immersion in ethanol (bottom). Markers represent the experimental data while the lines represent the fitted data according to the different equivalent circuits shown in insets.

and on Na-β''-alumina immersed in ethanol for an extended period of time (i.e. seven days to see the effect more clearly) shows that the crystal structure remains intact after ethanol exposure (see figure S4). A similar behavior is observed for the lithium solid electrolyte $Li_7La_3Zr_2O_{12}$ (LLZO) which is prone to surface protonation (H^+/Li^+ ion exchange) in contact to acidic solvents like ethanol resulting in a protonated phase with lower thermal stability compared to LLZO [46]. In the case of Na-β''-alumina, surface protonation impedes sodium-ion transport at the Na-β''-alumina interface, resulting in a pressure-independent interfacial resistance. While the achieved interfacial resistance of 25 Ω cm^2 is excellent compared to other systems with Na-β''-alumina ceramics, further studies should focus on minimizing the interfacial resistance associated with surface protonation of Na-β''-alumina, e.g. by avoiding protonation employing a low acidity, i.e. high pKa, solvent such as hexane as was demonstrated for LLZO in [43].

The impact of the densification pressure on the electrochemical performance of the full cell was further studied by rate performance measurements at increasing C-rates ranging from C/10 to 1 C between 2 V and 3.6 V. A stack pressure of 3.4 MPa was applied using a home-built pressure cell to avoid excessive void formation at the Na-β''-alumina/Na metal interface upon sodium stripping [47]. Rate tests shown in figure 3(a) indicate that increasing the densification from 3 MPa to 87 MPa doubles the first-cycle discharge capacity from 51 mAh g^{-1} to 103 mAh g^{-1}, respectively, and significantly decreases capacity losses during subsequent cycling. While the cell assembled with a low densification pressure of 3 MPa is unable to cycle at 1 C, the cell assembled at high densification pressure of 87 MPa retains a capacity of 25 mAh g^{-1}. The increase of first-cycle discharge capacity and improved rate capability with increasing densification pressure are consistent with the decrease in cell resistance observed in the Nyquist plots in figure 2(a). Cycling the cell assembled at 87 MPa after the rate test at C/10 yields almost the same discharge capacity of 100 mAh g^{-1}. These results indicate that the hydroborate secondary electrolyte acting as an interlayer maintains intimate contact between the Na-β''-alumina ceramic and the slurry-casted $NaCrO_2$ cathode. Overall, these results show that a dense hydroborate interlayer enabled by a densification pressure $\geqslant$70 MPa as a contacting medium is a promising approach enabling reversible capacity at competitive charging rates.

Based on these results, long-term cycling was performed with a cell assembled at a pressure of 70 MPa at 1 C rate with a cathode areal capacity of 0.4 mAh cm^{-2}. In order to minimize partial hydroborate oxidation during long-term cycling above its oxidative stability limit as determined in another study [39, 43], the upper cut-off voltage was set to 3.3 V. Cycling data shown in figures 3(b) and (c) indicate an initial discharge capacity of 42 mAh g^{-1}. Note that the higher initial capacity compared to the cell in figure 3(a) can be explained by the lower mass loading of 3.1 mg cm^{-2} compared to 6.5 mg cm^{-2} facilitating cycling at a faster rate (table S6). The cell features an excellent capacity retention of 88% after 100 cycles with a high Coulombic efficiency >99.9%. EIS performed before cycling and after the 1st and 100th cycle

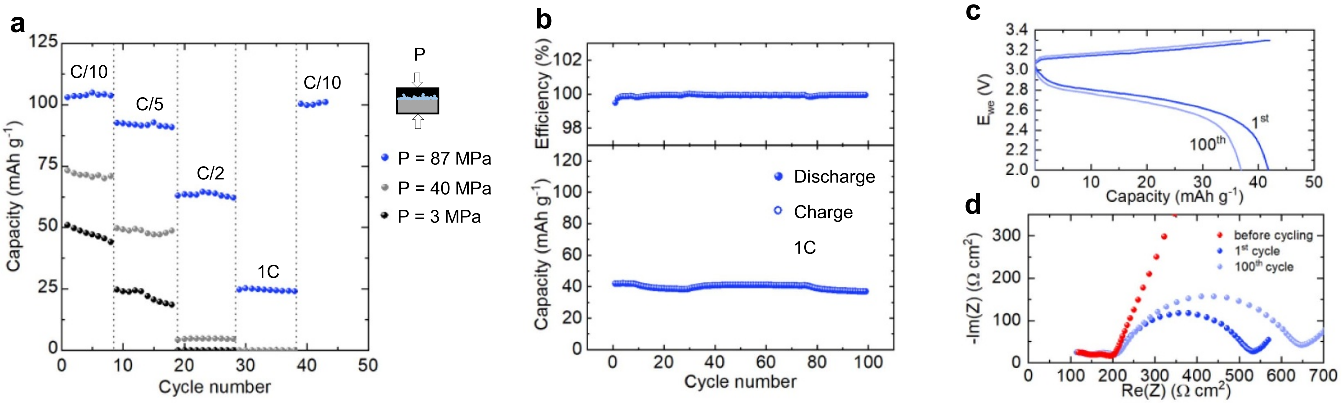

Figure 3. (a) Rate performance of all-solid-state cells assembled with different densification pressures and cycled under a stack pressure of 3.4 MPa. Capacities and C-rates are based on the weight of the cathode active material. (b) Electrochemical cycling stability and Coulombic efficiencies of a cell assembled at a densification pressure of 70 MPa and cycled under a stack pressure of 3.4 MPa. The cell was first activated for five cycles at C/10. (c) Galvanostatic charge/discharge profiles and (d) Nyquist plots of the same cell after the 1st and 100th cycle. The Nyquist plot of the same cell before cycling is shown together for comparison.

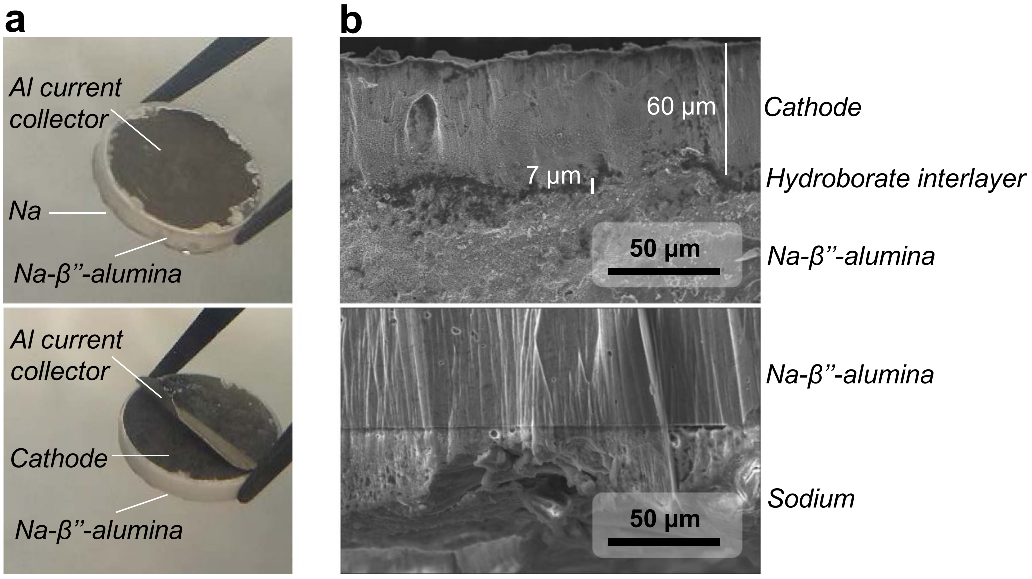

Figure 4. Post-mortem analysis performed on a cell assembled at a pressure ⩾70 MPa. (a) Photographs of a typical cell showing good cathode adherence on the Na-β''-alumina ceramic after detaching the Al current collector. (b) SEM cross-section images of the cathode/electrolyte (top) and anode/electrolyte interfaces (bottom).

shows that capacity fading is related to an increase in total cell resistance (figure 3(d)). While the contribution at 1 kHz related to the hydroborate/Na-β''-alumina interface stays constant, a new semi-circle at apex frequency of 7 Hz arises after the first charge/discharge cycle and increases with increasing cycling number. We attribute this new contribution to the cathode side, which involves the slow but ultimately non-negligible, partial hydroborate decomposition above its oxidative stability limit [39].

To analyze the mechanical contact of the Na-β''-alumina/cathode interface, we conducted post-mortem analysis on cells assembled at a densification pressure of 70 MPa. Mechanical adherence of the hydroborate-infiltrated cathode on the Na-β''-alumina was first assessed by manually detaching the aluminum current collector from the cell stack. Figure 4(a) shows that the aluminum foil is easily detached without ripping out $NaCrO_2$ particles from the cathode. Intimate contact between the Na-β''-alumina ceramic and the $Na_4(B_{12}H_{12})(B_{10}H_{10})$-infiltrated $NaCrO_2$ cathode was further confirmed by post-mortem SEM analysis of an ion-milled cell cross-section in figure 4(b) (top) after rate performance measurements. The SEM image shows a hydroborate interlayer of about 7 μm thickness between the Na-β''-alumina ceramic and the cathode. The absence of voids at the interface confirms that the hydroborate layer adheres well to both the $NaCrO_2$ cathode particles and the Na-β''-alumina ceramic. Note that the 20 μm-sized particle on the cathode as well as ion-milling deposits in the form of white aggregates are attributed to cutting deposits observed due to the fast ion-milling settings. The quality of the Na-β''-alumina/Na metal interface after long-term cycling was also investigated post-mortem using SEM shown in figure 4(b) (bottom). This reveals an intimate interface despite the presence of some voids mainly distributed away from the interface, which is typical after repeated sodium stripping and plating [47]. Note that the Na-β''-alumina morphology looks smoother in this last cross section compared to the Na-β''-alumina/cathode cross section which is due to a softer milling settings. As EIS spectra in figure 3(d) show nevertheless a stable Na-β''-alumina/Na metal interfacial resistance, we conclude that the applied pressure of 3.4 MPa during battery cycling is suitable to prevent excessive void formation at the Na-β''-alumina/Na metal interface at the applied current density of 0.4 mA cm^{-2}, which is in agreement with another study [47].

4. Conclusion

Based on the unique property of hydroborates to fully densify by cold pressing, we developed a novel all-solid-state sodium cell architecture to contact a slurry-casted porous $NaCrO_2$ cathode with a Na-β''-alumina ceramic solid electrolyte using a $Na_4(B_{12}H_{12})(B_{10}H_{10})$ hydroborate as interlayer and secondary electrolyte enabling a low interfacial resistance of 25 Ω cm^2. In a proof-of-concept 3 V full cell employing a $NaCrO_2$ cathode and a sodium metal anode, we demonstrate that the $Na_4(B_{12}H_{12})(B_{10}H_{10})$ interlayer maintains intimate contact between the Na-β''-alumina ceramic electrolyte and the $NaCrO_2$ cathode enabling stable cycling up to 1 C.

Towards fast-charging applications, the rate performance must be improved further e.g. by reducing the thickness of the Na-β''-alumina electrolyte. An alternative approach is to further decrease the pressure-independent interfacial resistance e.g. by using high pKa processing solvents such as hexane to prevent Na-β''-alumina protonation. For the development of high-energy all-solid-state batteries, future studies should also focus on using more stable hydroborates against electrochemical oxidation as secondary electrolyte such as $Na_4(CB_{11}H_{12})_2(B_{12}H_{12})$ in combination with high-voltage cathodes. High performance sodium cathodes competing with lithium cathodes (e.g. NMC811) need to be developed for the deployment of all-solid-state sodium batteries [36, 48–51]. Overall, this study shows first promising results in using soft hydroborates as a contacting medium between a hard brittle ceramic and a slurry-casted porous cathode and opens up new cell architecture for all-solid-state batteries.

Acknowledgments

Marie-Claude Bay acknowledges support from the BRIDGE Proof-of-Concept program under contract number 40B1-0_198678/2. The authors thank Roman Flury for his help with cells preparation and characterization as well as Ulrich Sauter for argon-ion cross-section milling and Léo Duchêne for SEM characterization of cathode active materials.

ORCID iDs

Marie-Claude Bay https://orcid.org/0000-0001-5149-562X
Rabeb Grissa https://orcid.org/0000-0003-2463-1766
Konstantin V Egorov https://orcid.org/0000-0002-9936-4802
Ryo Asakura https://orcid.org/0000-0002-9264-9493
Corsin Battaglia https://orcid.org/0000-0002-5003-1134

References

[1] Janek J and Zeier W G 2016 A solid future for battery development *Nat. Energy* **1** 16141
[2] Famprikis T, Canepa P, Dawson J A, Islam M S and Masquelier C 2019 Fundamentals of inorganic solid-state electrolytes for batteries *Nat. Mater.* **18** 1278
[3] Zhao C, Liu L, Qi X, Lu Y, Wu F, Zhao J, Yu Y, Hu Y-S and Chen L 2018 Solid-state sodium batteries *Adv. Energy Mater.* **8** 1703012
[4] Banerjee A, Wang X, Fang C, Wu E A and Meng Y S 2020 Interfaces and interphases in all-solid-state batteries with inorganic solid electrolytes *Chem. Rev.* **120** 6878
[5] Jiang Z, Han Q, Wang S and Wang H 2019 Reducing the interfacial resistance in all-solid-state lithium batteries based on oxide ceramic electrolytes *Chem. Electron. Chem.* **6** 2970
[6] Tan D H S, Banerjee A, Chen Z and Meng Y S 2020 From nanoscale interface characterization to sustainable energy storage using all-solid-state batteries *Nat. Nanotechnol.* **15** 170
[7] Sharafi A, Kazyak E, Davis A L, Yu S, Thompson T, Siegel D J, Dasgupta N P and Sakamoto J 2017 Surface chemistry mechanism of ultra-low interfacial resistance in the solid-state electrolyte $Li_7La_3Zr_2O_{12}$ *Chem. Mater.* **29** 7961
[8] Luo W *et al* 2017 Reducing interfacial resistance between garnet-structured solid-state electrolyte and Li-metal anode by a germanium layer *Adv. Mater.* **29** 1606042
[9] Tsai C-L, Roddatis V, Chandran C V, Ma Q, Uhlenbruck S, Bram M, Heitjans P and Guillon O 2016 $Li_7La_3Zr_2O_{12}$ interface modification for Li dendrite prevention *ACS Appl. Mater. Interfaces* **8** 10617
[10] Krauskopf T, Hartmann H, Zeier W G and Janek J 2019 Toward a fundamental understanding of the lithium metal anode in solid-state batteries—an electrochemo-mechanical study on the garnet-type solid electrolyte $Li_{6.25}Al_{0.25}La_3Zr_2O_{12}$ *ACS Appl. Mater. Interfaces* **11** 14463
[11] Wang M J, Choudhury R and Sakamoto J 2019 Characterizing the Li-solid-electrolyte interface dynamics as a function of stack pressure and current density *Joule* **3** 2165
[12] Xu W, Wang J, Ding F, Chen X, Nasybulin E, Zhang Y and Zhang J-G 2014 Lithium metal anodes for rechargeable batteries *Energy Environ. Sci.* **7** 513
[13] Lin D, Liu Y and Cui Y 2017 Reviving the lithium metal anode for high-energy batteries *Nat. Nanotechnol.* **12** 194
[14] Zhang S S 2018 Problem, status, and possible solutions for lithium metal anode of rechargeable batteries *ACS Appl. Energy Mater.* **1** 910
[15] Tang B, Jaschin P W, Li X, Bo S-H and Zhou Z 2020 Critical interface between inorganic solid-state electrolyte and sodium metal *Mater. Today* **41** 200
[16] Bay M-C, Wang M, Grissa R, Heinz M V F, Sakamoto J and Battaglia C 2020 Sodium plating from Na-β''-alumina ceramics at room temperature, paving the way for

fast-charging all-solid-state batteries *Adv. Energy Mater.* **10** 1902899

[17] Albertus P, Babinec S, Litzelman S and Newman A 2018 Status and challenges in enabling the lithium metal electrode for high-energy and low-cost rechargeable batteries *Nat. Energy* **3** 16–21

[18] Lacivita V, Wang Y, Bo S-H and Ceder G 2019 *Ab initio* investigation of the stability of electrolyte/electrode interfaces in all-solid-state Na batteries *J. Mater. Chem.* A **7** 8144

[19] Fertig M P, Skadell K, Schulz M, Dirksen C, Adelhelm P and Stelter M 2022 From high- to low-temperature: the revival of sodium-beta alumina for sodium solid-state batteries *Batter. Supercaps* **5** e202100131

[20] Dustmann C-H 2004 Advances in ZEBRA batteries *J. Power Sources* **127** 85

[21] Sudworth J L 2001 The sodium/nickel chloride (ZEBRA) battery *J. Power Sources* **100** 149

[22] Sheng O, Jin C, Ding X, Liu T, Wan Y, Liu Y, Nai J, Wang Y, Liu C and Tao X 2021 A decade of progress on solid-state electrolytes for secondary batteries: advances and contributions *Adv. Funct. Mater.* **31** 2100891

[23] Yamauchi H, Ikejiri J, Sato F, Oshita H, Honma T and Komatsu T 2019 Pressureless all-solid-state sodium-ion battery consisting of sodium iron pyrophosphate glass-ceramic cathode and β''-alumina solid electrolyte composite *J. Am. Ceram. Soc.* **102** 6658

[24] Yamauchi H, Ikejiri J, Tsunoda K, Tanaka A, Sato F, Honma T and Komatsu T 2020 Enhanced rate capabilities in a glass-ceramic-derived sodium all-solid-state battery *Sci. Rep.* **10** 9453

[25] Liu L, Qi X, Ma Q, Rong X, Hu Y-S, Zhou Z, Li H, Huang X and Chen L 2016 Toothpaste-like electrode: a novel approach to optimize the interface for solid-state sodium-ion batteries with ultralong cycle life *ACS Appl. Mater. Interfaces* **8** 32631

[26] Zhao K, Liu Y, Zhang S, He S, Zhang N, Yang J and Zhan Z 2016 A room temperature solid-state rechargeable sodium ion cell based on a ceramic Na-β''-Al_2O_3 electrolyte and $NaTi_2(PO_4)_3$ cathode *Electrochem. commun.* **69** 59

[27] Wu T, Wen Z, Sun C, Wu X, Zhang S and Yang J 2018 Disordered carbon tubes based on cotton cloth for modulating interface impedance in β''-Al_2O_3-based solid-state sodium metal batteries *J. Mater. Chem.* A **6** 12623–9

[28] Chi X, Hao F, Zhang J, Wu X, Zhang Y, Gheytani S, Wen Z and Yao Y 2019 A high-energy quinone-based all-solid-state sodium metal battery *Nano Energy* **62** 718

[29] Lei D *et al* 2019 Cross-linked beta alumina nanowires with compact gel polymer electrolyte coating for ultra-stable sodium metal battery *Nat. Commun.* **10** 4244

[30] Liu Z, Wang X, Chen J, Tang Y, Mao Z and Wang D 2021 Gel polymer electrolyte membranes boosted with sodium-conductive β-alumina nanoparticles: application for Na-ion batteries *ACS Appl. Energy Mater.* **4** 623

[31] Duchêne L, Kühnel R-S, Rentsch D, Remhof A, Hagemann H and Battaglia C 2017 A highly stable sodium solid-state electrolyte based on a dodeca/deca-borate equimolar mixture *Chem. Commun.* **53** 4195

[32] Duchêne L, Remhof A, Hagemann H and Battaglia C 2020 Status and prospects of hydroborate electrolytes for all-solid-state batteries *Energy Storage Mater.* **25** 782

[33] Asakura R, Duchêne L, Kühnel R-S, Remhof A, Hagemann H and Battaglia C 2019 Electrochemical oxidative stability of hydroborate-based solid-state electrolytes *ACS Appl. Energy Mater.* **2** 6924

[34] Brighi M, Murgia F and Černý R 2022 Mechanical behavior and dendrite resistance of closo-hydroborate solid electrolyte *Adv. Mater. Interfaces* **9** 2101254

[35] Duchêne L, Kim D H, Song Y B, Jun S, Moury R, Remhof A, Hagemann H, Jung Y S and Battaglia C 2020 Crystallization of closo-borate electrolytes from solution enabling infiltration into slurry-casted porous electrodes for all-solid-state batteries *Energy Storage Mater.* **26** 543

[36] Asakura R, Reber D, Duchêne L, Payandeh S, Remhof A, Hagemann H and Battaglia C 2020 4 V room-temperature all-solid-state sodium battery enabled by a passivating cathode/hydroborate solid electrolyte interface *Energy Environ. Sci.* **13** 5048

[37] Bay M-C, Heinz M V F, Figi R, Schreiner C, Basso D, Zanon N, Vogt U F and Battaglia C 2019 Impact of liquid phase formation on microstructure and conductivity of Li-stabilized Na-β''-alumina ceramics *ACS Appl. Energy Mater.* **2** 687

[38] Bay M-C, Heinz M V F, Danilewsky A N, Battaglia C and Vogt U F 2021 Analysis of c-lattice parameters to evaluate Na_2O loss from and Na_2O content in β''-alumina ceramics *Ceram. Int.* **47** 13402

[39] Asakura R, Duchêne L, Payandeh S, Rentsch D, Hagemann H, Battaglia C, Remhof A and Remhof A 2021 Thermal and electrochemical interface compatibility of a hydroborate solid electrolyte with 3 V-class cathodes for all-solid-state sodium batteries *ACS Appl. Mater. Interfaces* **13** 55319

[40] Yu C-Y, Park J-S, Jung H-G, Chung K-Y, Aurbach D, Sun Y-K and Myung S-T 2015 $NaCrO_2$ cathode for high-rate sodium-ion batteries *Energy Environ. Sci.* **8** 2019

[41] Nafe D, Von Nacro Z K and Hoppe R 1989 Über den alpha-$NaFeO_2$-Typ Zur Kenntnis von $NaCrO_2$ und $KCrO_2$ *Z. Anorg. Allg. Chem.* **568** 151

[42] Komaba S, Takei C, Nakayama T, Ogata A and Yabuuchi N 2010 Electrochemical intercalation activity of layered $NaCrO_2$ vs. $LiCrO_2$ *Electrochem. Commun.* **12** 355

[43] Duchêne L, Kühnel R-S, Stilp E, Cuervo Reyes E, Remhof A, Hagemann H and Battaglia C 2017 A stable 3 V all-solid-state sodium–ion battery based on a closo-borate electrolyte *Energy Environ Sci.* **10** 2609

[44] Lilley E and Strutt J E 1979 Bulk and grain boundary ionic conductivity in polycrystalline β''-alumina *Phys. Status Solidi* **54** 639

[45] Kim J H, Shin E C, Cho D C, Kim S, Lim S, Yang K, Beum J, Kim J, Yamaguchi S and Lee J S 2014 Electrical characterization of polycrystalline sodium beta$''$-alumina: revisited and resolved *Solid State Ion.* **264** 22

[46] Grissa R, Payandeh S, Heinz M and Battaglia C 2021 Impact of protonation on the electrochemical performance of $Li_7La_3Zr_2O_{12}$ Garnets *ACS Appl. Mater. Interfaces* **13** 14700

[47] Spencer Jolly D, Ning Z, Darnbrough J E, Kasemchainan J, Hartley G O, Adamson P, Armstrong D E J, Marrow J and Bruce P G 2020 Sodium/Na β'' alumina interface: effect of pressure on voids *ACS Appl. Mater. Interfaces* **12** 678

[48] Gu Z-Y, Guo J-Z, Sun Z-H, Zhao X-X, Wang X-T, Liang H-J, Wu X-L and Liu Y 2021 Air/water/temperature-stable cathode for all-climate sodium-ion batteries *Cell Rep. Phys. Sci.* **2** 100665

[49] Gu Z, Guo J, Cao J, Wang X, Zhao X, Zheng X, Li W, Sun Z, Liang H and Wu X 2022 An advanced high-entropy fluorophosphate cathode for sodium-ion batteries with increased working voltage and energy density *Adv. Mater.* **34** 2110108

[50] Tarascon J-M 2020 Na-ion versus Li-ion batteries: complementarity rather than competitiveness *Joule* **4** 1616

[51] Mariyappan S, Wang Q and Tarascon J M 2018 Will sodium layered oxides ever be competitive for sodium ion battery applications? *J. Electrochem. Soc.* **165** A3714